# Weierstraß-Institut für Angewandte Analysis und Stochastik Leibniz-Institut im Forschungsverbund Berlin e. V.

Preprint ISSN 2198-5855

# Low-frequency fluctuations in semiconductor lasers with delayed optical feedback

Mindaugas Radziunas<sup>1</sup>, Deborah M. Kane<sup>2</sup>

submitted: November 3, 2025

Weierstrass InstituteAnton-Wilhelm-Amo-Str. 3910117 BerlinGermany

E-Mail: mindaugas.radziunas@wias-berlin.de

Research School of Physics Australian National University Canberra, ACT 2600 Australia E-Mail: Deb.Kane@anu.edu.au

No. 3226 Berlin 2025



2020 Mathematics Subject Classification. 78A60, 37N20, 78-10, 78M22, 78M34.

Key words and phrases. Semiconductor laser, optical feedback, traveling wave model, optical modes, mode analysis, low-frequency fluctuations, simulations.

The authors thank Professor Cristina Masoller for discussions.

Edited by
Weierstraß-Institut für Angewandte Analysis und Stochastik (WIAS)
Leibniz-Institut im Forschungsverbund Berlin e. V.
Anton-Wilhelm-Amo-Straße 39
10117 Berlin
Germany

Fax: +49 30 20372-303

E-Mail: preprint@wias-berlin.de
World Wide Web: http://www.wias-berlin.de/

# Low-frequency fluctuations in semiconductor lasers with delayed optical feedback

Mindaugas Radziunas, Deborah M. Kane

#### **Abstract**

Low-frequency fluctuations in a semiconductor laser with optical feedback system are analyzed with a traveling wave model, and the concepts of instantaneous and compound cavity modes. Compound-cavity mode curves, including their height and width characteristics in the frequency/carrier-density-offset plane, provide good estimates of parameter ranges where low-frequency fluctuations occur. These ranges cover a larger part of the parameter space than is commonly realized.

Research on the semiconductor laser (SL) with delayed optical feedback (SLDOF), both experimental and theoretical, has been key to nonlinear laser dynamics studies over several decades [1, 2, 3]. In this setup, the reinjection from the external cavity (EC),  $F_{\rm i}$ , is defined by the emitted field,  $F_{\rm e}$ , which is delayed by the EC round-trip time  $\tau$  and scaled by the complex feedback factor  $\kappa e^{i\phi}$  (Fig. 1). Within this broad field, study of low frequency fluctuations (LFFs), mostly near the threshold current  $I_{\rm th}$  of the free running SL and with optical feedback near the coherence collapse boundary, have been prolific (e.g. [4, 5, 6, 7]). The foci have been mostly scoping LFF regimes and understanding their origin as due to deterministic chaos or stochastic drivers.

LFFs manifest as sudden, quasi-periodic changes in chaotic operating states and a slow return to prior conditions. LFF frequencies ( $\nu_{\rm lff}$ ) lie well below those of the system's intrinsic oscillations. These include the solitary-laser resonance (SLR) beat frequency  $\nu_{\rm sl}$  (hundreds of GHz, linked to the SL diode cavity round-trip time  $\tau_0$ ), the relaxation-oscillation frequency  $\nu_{\rm ro}$  (tied to carrier-photon dynamics and pump current, typically a few GHz well above  $I_{\rm th}$ ), and the compound-cavity mode (CCM) spacing frequency  $\nu_{\rm ec} \approx \tau^{-1}$  (sub-GHz for the long cavity case here). A 2013 review [3] summarized the key insights into LFFs in SLDOFs known at that time. Until then, it was difficult to measure the chaotic, fast-timescale (tens of picoseconds) component of the dynamics, as real-time detection was typically limited to bandwidths below 100 MHz. Thus, only the slower LFFs were accessible in real time, while spectral measurements were used to probe the higher-frequency behavior. These constraints likely led to LFFs being reported as a regime of operation, which is appropriate when LFFs dominate the radiofrequency (RF) spectrum obtained from fully time-resolved power measurement. LFF regimes have been defined as those where the low-frequency peak in the RF spectrum exceeds other components by at least 10 dB [8]. However, LFFs can exist without producing a *distinct* low-frequency RF-peak, and they occur over a much larger parameter range than is commonly appreciated. Some

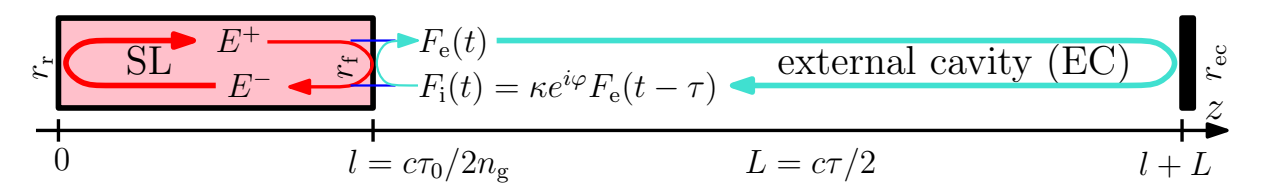


Figure 1: Schematic of a SLDOF, consisting of the SL and the EC.

studies examined LFFs in SLDOFs operating well above  $I_{\rm th}$  and under strong optical feedback. LFFs were experimentally observed between the coherence collapse and the single-frequency regions [9]. At higher injection currents,  $I\gg I_{\rm th}$ , a transition from power dropouts to jump-ups was reported.

Another system with filtered optical feedback was used to study LFFs [10] for  $\kappa \leq 0.12$  and  $I \leq 8I_{\rm th}$ . LFFs with power dropouts, jump-ups, and none of them were found. Jump-ups were prevalent, and the results were similar to [9]. A study of a quantum-dot (QD)-based SLDOF [11] stated that LFFs at high I and  $\kappa$  differed from those in quantum-well (QW)-based systems "because LFF dynamics appear only for small injection currents close to the lasing threshold" for QWs. While QD-system LFFs may indeed differ, the reason is different. This misconception has clear historical roots but should be corrected.

Our traveling wave (TW) model-based studies [12, 13] of a Fabry–Perot SLDOF, experimentally investigated in [14], revealed a strong low-frequency RF peak – a clear signature of LFFs. In [15], the LFF regimes were analyzed using an advanced mode-analysis technique that enabled time–frequency representations of LFF events and explained the resonances observed in spectral representations. In this letter, we employ mode analysis to quickly predict the feedback ranges that support LFFs, eliminating the need for time- and memory-intensive simulations.

Below we explore the TW model, defining the spatiotemporal evolution of the slowly varying complex field vector-function  $\Psi(z,t)$  and the real carrier density distribution N(z,t):

$$-i\partial_t \Psi(z,t) = \mathcal{H}(\beta(N,\varepsilon P))\Psi + F_{\rm sp}(z,t), \quad z \in \mathrm{SL} \cup \mathrm{EC}, \tag{1a}$$

$$\frac{d}{dt}N(z,t) = \mathcal{N}(I,N,\Psi), \quad z \in \text{SL}. \tag{1b}$$

The matrix operator  $\mathcal{H}$  depends on the complex propagation factor  $\beta$ , includes the spatial derivatives  $\partial_z$ , and incorporates reflection—transmission conditions set by the rear- and front-facet and the EC mirror reflectivities  $r_{\rm r}$ ,  $r_{\rm f}$ , and  $r_{\rm ec}$  (see Fig. 1). Assuming  $\beta$  is constant in the EC, (1a) yields the relation  $E^-(l^+,t)=\kappa e^{i\varphi}E^+(l^+,t-\tau)$  linking the reinjected and emitted fields  $E^-(l^+,t)=F_{\rm i}$  and  $E^+(l^+,t)=F_{\rm e}$ , evaluated just beyond the SL front facet ( $z=l^+$ ). Here,  $E^+$  and  $E^-$  are forward- and back-propagating components of  $\Psi$ . Within the SL,  $\beta$  depends on N(z,t) and the local photon density  $P(z,t)\propto |E^+|^2+|E^-|^2$ , with  $\varepsilon$  denoting the nonlinear gain compression factor. A linear dependence of  $\beta$  on N is used, with its real and imaginary parts linked through the linewidth enhancement factor  $\alpha_{\rm H}=3.5$ . We set  $\varphi=0$ ,  $r_{\rm f}=\sqrt{0.05}$ , l=0.3 mm, and  $\tau=4.5$  ns. A detailed formulation of the TW model and all remaining parameters can be found in [15] and Appendix. The SLDOF system modeled is close to one for which a comprehensive output power time series dataset exists to facilitate connection with experiment [14].

As a first look at the system's LFF dynamics, Fig. 2 compares simulations at low bias ( $I\approx I_{\rm th}$ ) and moderate feedback ( $\kappa=0.02$ ), with those at higher bias ( $I\approx 2.2\,I_{\rm th}$ ) and strong feedback ( $\kappa=0.2$ ). Most LFF studies in SLDOF systems focus on conditions similar to the former case,  $I\lesssim I_{\rm th}$  [4, 5], where the feedback reduces the effective threshold, enabling sustained lasing and inducing LFFs. These manifest as abrupt drops in emitted power  $|F_{\rm e}(t)|^2$  and spatially averaged field power  $\bar{P}(t)$ , blue traces in Figs. 2(a,c), consistent with experimental observations [4, 5, 6, 7, 3]. Intrinsic oscillations at frequencies  $\nu\gg\nu_{\rm lff}$  obscure the field power time traces in time-domain calculations. We apply low-pass filters (LPFs) to reveal the underlying slow dynamics, as shown in Figs. 2(a,c). Filtering only  $\nu_{\rm sl}\approx130\,{\rm GHz}$  oscillations with a  $30\,{\rm GHz}$  LPF (red curves) provides a moderate amplitude reduction in long-time span representations (left part of the diagrams). Applying a  $0.2\,{\rm GHz}$  LPF (black curves) removes even the CCM-beating oscillations ( $\nu_{\rm ec}\approx0.22\,{\rm GHz}$ ), clearly revealing LFF power drops.

Identifying LFF power changes becomes more difficult if operating well-above-threshold, as shown in Figs. 2(b,d) for  $I\approx 2.2\,I_{\rm th}$ . First, the spatially averaged (thus unmeasurable) power levels during and just before the LFF event, when the SLDOF operates close to the maximal gain mode (MGM) [15], are less distinguishable. As shown by the black curves in Figs. 2(c) and (d),  $\bar{P}_{\rm lff}/\bar{P}_{\rm mg}\approx 0.13$  and

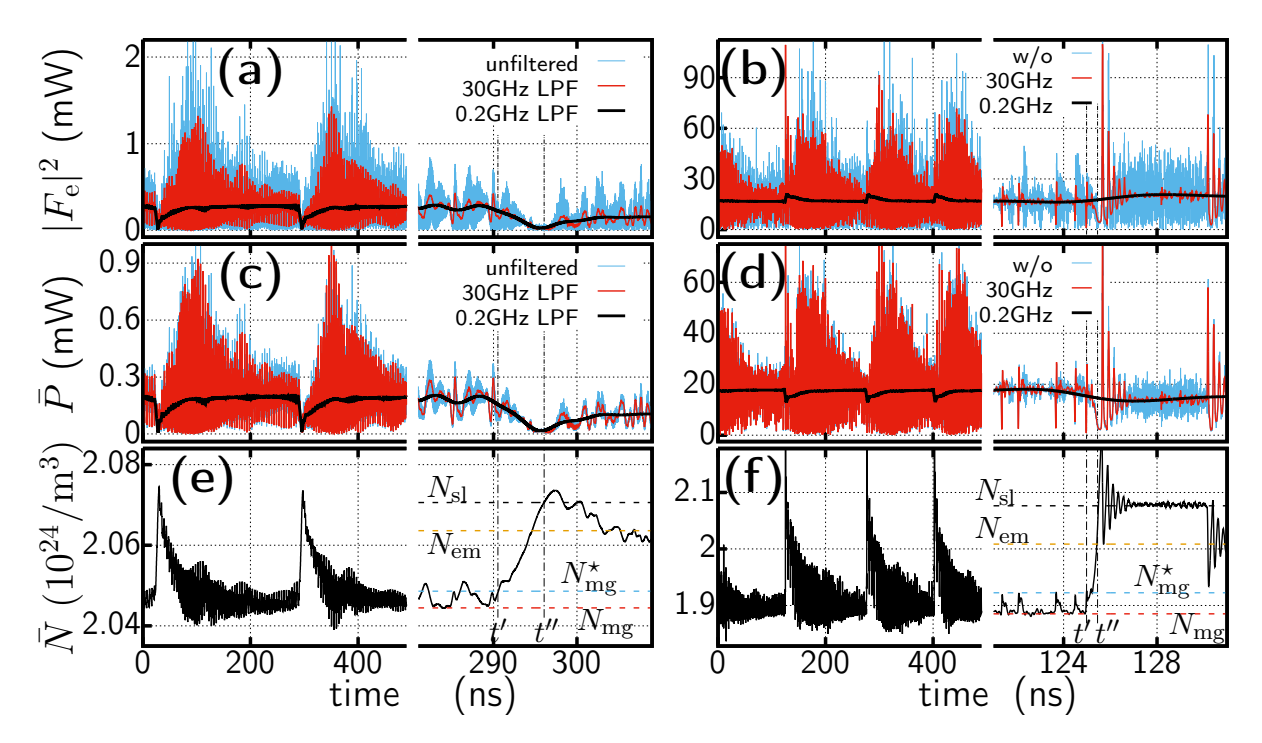


Figure 2: LFFs in an SLDOF operating at  $(I, \kappa) = (25 \, \mathrm{mA}, 0.02)$  (left) and  $(55 \, \mathrm{mA}, 0.2)$  (right). Time traces of the emitted (a,b) and spatially-averaged field intensities (c,d) without (blue) and after a  $30 \, \mathrm{GHz}$  LPF (red) or a  $0.2 \, \mathrm{GHz}$  LPF (black); and the spatially-averaged carrier density (e,f).

0.78, respectively. Second, LFF events can manifest as sudden power *jumps* rather than drops in the (measurable) emitted field power, see the black curve in Fig. 2(b). This emission enhancement under reduced feedback [13] is available in spatially distributed models and is expected experimentally. It is difficult to achieve in the Lang-Kobayashi (LK) models [16]. In simulations, LFFs show up clearly in carrier density time traces. Figs. 2(e,f) show sudden rises in spatially-averaged carrier density  $\bar{N}(t)$ . t' to t'' is the climb time to reach the solitary-SL threshold density  $N_{\rm sl}$  initiating the  $\nu_{\rm ro}$ -frequency oscillations around that level within one delay period  $\tau$ . Both depend on I. Subsequently,  $\bar{N}(t)$  gradually relaxes toward the MGM level  $N_{\rm mg}$ , where new LFF events can occur.

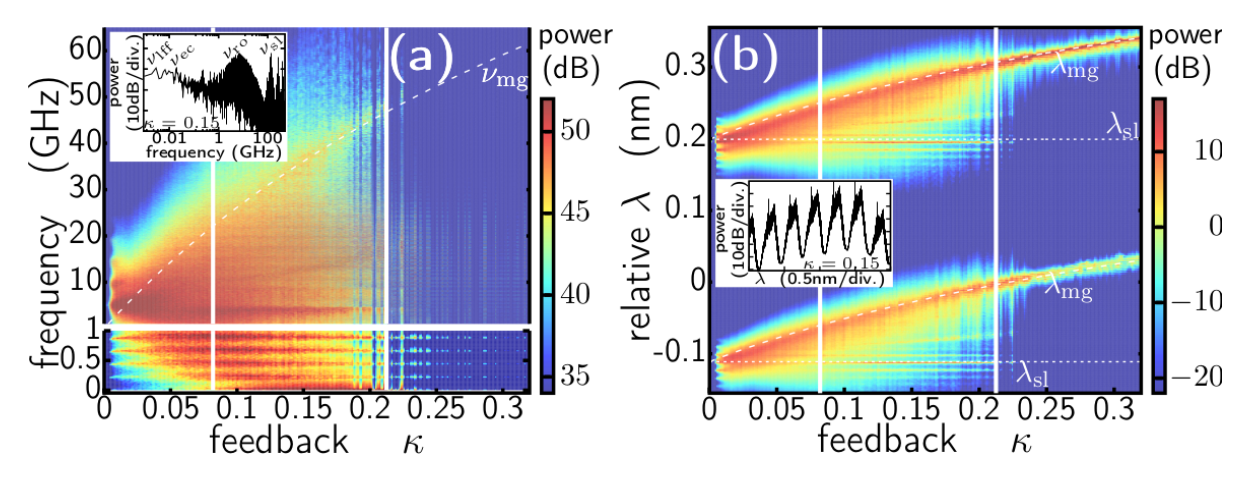


Figure 3: RF (a) and optical (b) spectrum mappings of the SLDOF for  $I=55\,\mathrm{mA}$  and an increased  $\kappa$ , color-coded on a dB scale. Insets: spectra with a log-scale frequency axis (left) and an extended wavelength range (right) for  $\kappa=0.15$ .

Spectral representations offer an alternative for detecting LFFs. Parts of the simulated RF and optical

spectra for up-tuned  $\kappa$  are shown in Figs. 3(a) and (b), respectively. Approximate LFF ranges are marked by vertical white bars. For each  $\kappa$ , we calculated  $1.5\,\mu$ s transients, analyzed the last  $1\,\mu$ s, and increased  $\kappa$  by 0.001. LFFs manifest as strong (red) peaks in the RF spectra (panel (a)) at sub-  $0.1\,\mathrm{GHz}$  frequencies. In optical spectra (panel (b)), LFFs are indicated by a broadened peak reaching the MGM wavelength,  $\lambda_{\mathrm{mg}}$ , where the system resides much of the time, and a sharper peak at the SLR,  $\lambda_{\mathrm{sl}}$ , activated during brief LFF events. When undamped, these two peaks recur near multiple SLRs, see inset in panel (b).

To gain deeper insight into the LFF mechanism, we analyze the *instantaneous modes* – pairs of complex eigenfrequencies  $\Omega$  and eigenvectors  $\Theta(z)$  that, for a fixed  $\beta(z,t)$  at a given time t, solve the spectral problem induced by operator  $\mathcal{H}$ . Expanding the field in terms of time-varying normalized eigenvectors  $\Theta_k(z;\beta(z,t))$  yields ODEs for the complex mode amplitudes  $f_k(t)$  [15]. Mode coupling terms scale with  $\frac{d\bar{N}}{dt}$  (alternating in sign with time) and with the inverse of the mode frequency separation, which is typically limited by  $\tau/2\pi$ . This coupling is usually weak, such that  $\Re\Omega$  and  $\Im\Omega$  reliably describe each mode's instantaneous optical frequency and amplification or damping rate, even in the presence of other undamped modes. Only a few instantaneous modes, when being close to the exceptional point, can have a reduced frequency separation and experience large short-time coupling.

When  $\Omega$  is real, the mode is neither damped nor amplified and may define a steady state, or CCM of the SLDOF. These states are typically well approximated by the CCMs of a simplified TW model obtained by neglecting gain dispersion and nonlinear compression ( $\varepsilon=0$ ), replacing N(z,t) with its spatial average  $\bar{N}(t)$ , and averaging (1b) [17, 15]. In contrast to the general case, the real pairs  $(\Omega,\bar{N})$  obtained from the reduced field equations, or their offsets  $(\Delta\Omega,\Delta\bar{N})$  from a SLR  $(\omega_{\rm sl},N_{\rm sl})$ , are sufficient to determine the steady states [17]. For fixed  $\kappa$ , CCM curves, analogs of the external-cavity-mode (ECM) ellipses of the LK model, are defined in  $(\Re\Delta\Omega,\Delta\bar{N})$  domain by  $\Delta\omega=(\Delta\omega_{\rm mg}/\Delta N_{\rm mg})\Delta\bar{N}\pm\frac{W(\Delta\bar{N})}{2}\mod\frac{2\pi}{\tau_0}$ . The curve width  $W(\Delta\bar{N})$  and MGM positions  $(\Delta\omega_{\rm mg},\Delta N_{\rm mg})$  are given analytically [15], while later used curve height  $H(\Delta\omega)$  must be found numerically. Each curve contains individual CCMs separated in frequency by about  $2\pi/\tau$ . For more details on instantaneous modes, CCM curves, and available formulas see Appendix.

Fig. 4 shows parts of CCM curves near a single SLR (black box) for several  $\kappa$ . In contrast to the LK-model, the curves surround or bypass multiple SLRs. Instantaneous modes inside (gray shading for  $\kappa=0.15$ ) or outside the loops have negative or positive  $\Im\Omega$  (i.e., damping). Except for an exceptional mode (EM),  $\Re\Omega$  varies weakly with  $\bar{N}$ , maintaining a spacing of about  $\tau^{-1}$  to its neighbors. Amplification is strongest when  $(\Re\Omega,\bar{N})$  lies near the loop diagonal, with maximal gain for regular modes slightly above the SLR. Each regular mode defines two CCMs,  $(\omega_s,\bar{N}_s)$  and  $(\omega_s^\star,\bar{N}_s^\star)$ , with similar frequencies on the lower and upper loop branches. The two states are analogs of the "mode" (node-type) and the "antimode" (saddle-type) ECMs of the LK model. An example of a node-type CCM induced by a regular mode is the MGM (black up-triangle). In contrast, the EM follows the thin dotted line with  $\Im\Omega$  decreasing along its path. Below  $N_{\rm sl}$ , the EM at  $\sim 48\,{\rm GHz}$  behaves like a regular mode and defines a node-type CCM  $(\omega_{\rm em},N_{\rm em})$  (black down-triangle), with  $\omega_{\rm em}$  only slightly above  $\omega_{\rm sl}$ . Unlike regular modes, the EM does not form a dual CCM: once  $\bar{N}$  exceeds  $\bar{N}_{\rm sl}$ , it bypasses nearby located complex  $\Omega$  of another mode and continues along the CCM loop's diagonal (see Fig. 3(b) in [15] for more details). For  $\bar{N}\gtrsim N_{\rm sl}$ , the EM's complex frequency can approach those of neighboring modes, leading to strong short-time coupling and intensity exchange between them.

The EM-induced CCMs have  $\Delta\omega_{\rm em}\approx 0$ . By neglecting  $\Delta\omega_{\rm em}$ , we can relate the CCM curve's height estimates at two frequency offsets,  $H'=H(-W(\Delta N_{\rm em}))$  and  $H''=H(\Delta\omega_{\rm mg})$  (green and red

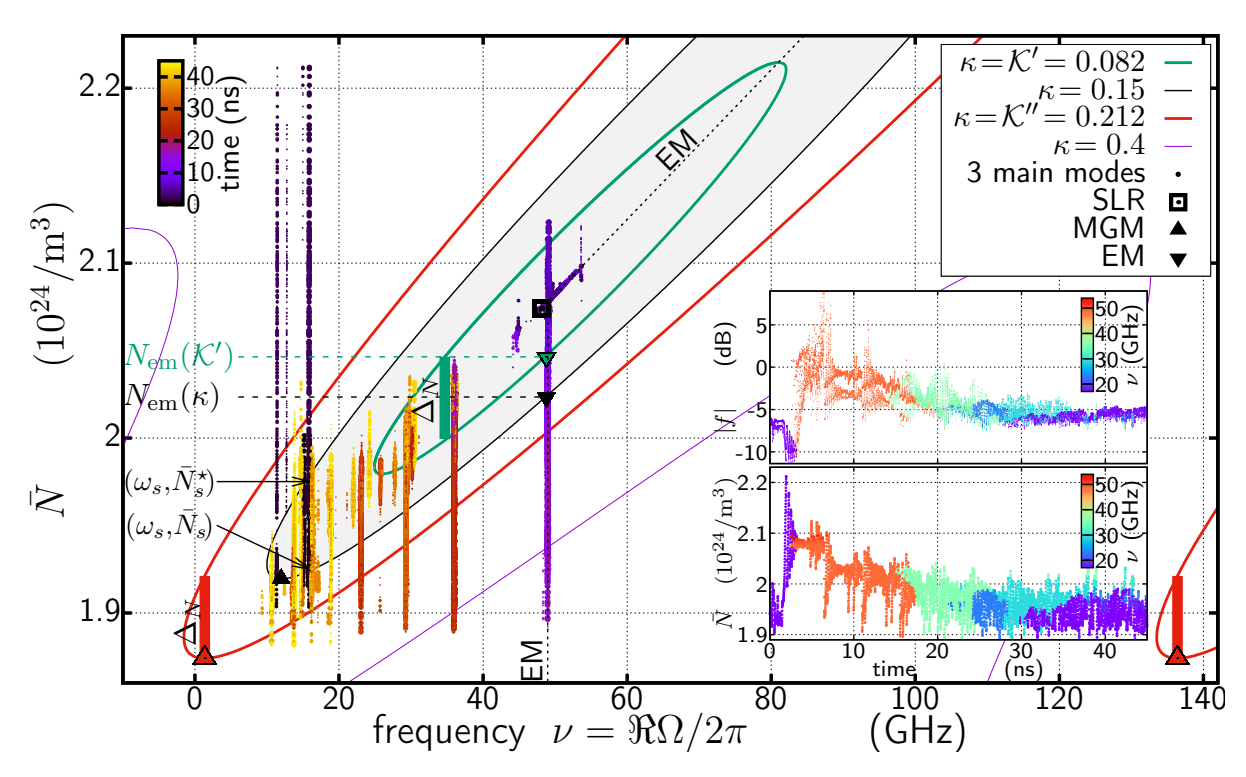


Figure 4: Three main modes (dots) near a single SLR during the LFF event in the  $\Re\Omega/\bar{N}$  domain with a color-coding of the time instants. Insets show corresponding time-traces of those mode amplitudes and  $\bar{N}(t)$ , colored by mode frequencies. Solid: CCM curves for selected  $\kappa$ . Green/red: curves at the minimal and maximal  $\kappa$  where LFFs are expected. Thick vertical bars: expected initiation of LFFs by fluctuating  $\bar{N}$  with maximal overshoot  $\Delta_N$ . Box and triangles: special modes.

vertical bars for  $\kappa = \mathcal{K}'$  and  $\mathcal{K}''$  in Fig. 4) by

$$\begin{cases} W(\Delta N_{\rm em}) + 2(\Delta \omega_{\rm mg}/\Delta N_{\rm mg})\Delta N_{\rm em} = 0\\ 2(\Delta \omega_{\rm mg}/\Delta N_{\rm mg})(\Delta N_{\rm em} + H') = W(\Delta N_{\rm em} - H') \end{cases} , \tag{2a}$$

$$2(\Delta\omega_{\rm mg}/\Delta N_{\rm mg})H''\Delta\omega_{\rm mg} = W(H'' + \Delta N_{\rm mg}). \tag{2b}$$

When defined,  $H(\Delta\omega_s,\kappa)\approx \bar{N}_s^\star - \bar{N}_s$ , increases with both  $\kappa$  and  $\omega_s\in [\omega_{\rm mg},\omega_{\rm sl}]$ . In contrast to the LK model, it is undefined if  $\kappa$  significantly exceeds  $|r_{\rm f}|$  and dual "antimodes" do not exist.

Within the LK-model framework [5, 6], LFFs are explained by chaotic trajectories crossing the stable manifold of an antimode  $(\omega_s^\star, \bar{N}_s^\star)$ , which triggers a rapid excursion along the unstable manifold to high carrier densities, accompanied by sudden power drops. Large time lags between LFF events arise from the slow relaxation back towards the MGM, where the trajectory may again cross an antimode's stable manifold. Our TW modeling confirms this scenario, though we do not construct CCM manifolds explicitly. To explain the LFFs, we use Figs. 2(c-f) and Fig. 4 (case  $\kappa=0.15$ , represented by the colored dots, black CCM curve, and insets). A typical LFF consists of the following stages:

- (i) Just before the LFF event, the EM and neighboring modes are damped, while  $\bar{N}(t)$  and  $\Re\Omega$  of the main modes are close to  $(\omega_s,\bar{N}_s)$  (and the MGM) on the lower part of the CCM curve, see black dots and up-triangle in Fig. 4. In Figs. 2(e,f) rightside,  $\bar{N}(t)$  oscillates just above the red horizontal line,  $N_{mg}$ .
- (ii) A fluctuating  $\bar{N}(t)$  exceeds  $\bar{N}_s^\star$  of the dual CCM on the upper CCM loop, see Fig. 4 and the light blue line at the instant t' in Figs. 2(e,f) rightside, initiating damping of the  $\omega_s$ -modes.

- (iii) The still dominant  $\omega_s$ -modes are damped,  $\bar{P}$  decays, and  $\bar{N}$  grows, until it reaches and exceeds  $N_{\rm sl}$ , see Figs. 2(c-f) within the time interval [t',t'']. To see a power drop, inspect the blue or red curves in panel (d). The dominance of the  $\omega_s$ -modes during this transition is indicated by the black (up to  $4\,{\rm ns}$ ) dots in Fig. 4 and the violet (about  $17\,{\rm GHz}$ ) dots in the insets.
- (iv) Increasing  $\bar{N}$  amplifies modes with  $\Re\Omega>\omega_s$ . However, it is the EM and its neighbors with the smallest  $\Im\Omega$  that experience the largest growth over a short time window and start to dominate shortly after  $\bar{N}$  exceeds  $N_{\rm sl}$ . Fig. 4 shows this with the first appearance of dark dots near the SLR and the switch between violet and red colors in the insets. From that point on, the fields entering the EC are primarily determined by  $\omega_{\rm em}$ -modes.
- (v) For about au-time slot,  $\bar{N}(t)$  and the main mode frequencies remain close to those of the SLR, see oscillations of  $\bar{N}(t)$  around the black line behind t'' in Figs. 2(e,f).  $\omega_{\rm em}$ -modes grow (red dots at [4,8] ns in the top inset of Fig. 4), sharing their intensity due to the large contributions from  $K_{k,l}$ .
- (vi) The  $\omega_{\rm em}$ -modes-determined reinjected fields, mainly, force the reduction of  $\bar{N}(t)$  toward  $N_{\rm em}$ , orange line in Figs. 2(e,f). This drop implies the amplification of lower-frequency modes (dots at about  $36~{\rm GHz}$  in Fig. 4). The  $\omega_{\rm em}$ -modes remain important for another  $\tau$ -order time slot (see the switches between the red and green color dots within [15,20] ns in the insets of Fig. 4).
- (vii) The previous step is repeated with the updated frequency of the reinjected field leading to a further reduction of  $\bar{N}$  and the dominating frequencies. The evolution of dots (as indicated by their time calibrated color) in Fig. 4 and its insets shows involvement of modes with decaying frequencies until  $\omega_s$ -modes dominate again and a new LFF event can be realized.

Thus, to initiate an LFF event once the  $\omega_s$ -modes dominate, the following must hold: (A)  $\omega_{\rm em}$ -modes are damped; (B) fluctuating  $\bar{N}(t)$  reaches and crosses the  $\bar{N}_s^\star$  level; and (C) as  $\bar{N}$  rises to  $N_{\rm sl}$  and beyond,  $\omega_s$ -modes are damped while  $\omega_{\rm em}$ -modes are amplified. To formalize these requirements, we define the maximal overshoot  $\Delta_N = \max_{t,r} \bar{N}(t) - \bar{N}_r$  of  $\bar{N}(t)$  when  $\omega_r$ -modes dominate (the trajectory fluctuates around the CCMs  $(\omega_r, \bar{N}_r)$ ) and the system is before or well after an LFF event. The conditions (A)-(C) for initiating the LFF at  $(\omega_s, \bar{N}_s)$  read as

$$\bar{N}_s + \Delta_N \le N_{\rm em}, \quad \Delta_N \ge H(\Delta\omega_s), \quad \omega_{\rm mg} \le \omega_s < \omega_{\rm sl}$$
 (3a)

$$\Rightarrow \Delta \omega_{\rm mg} \le -W(\Delta N_{\rm em}) \Rightarrow H'' \le \Delta_N \le H'.$$
 (3b)

The first and second conditions in (3a) ensure (A) during N fluctuations and (B), respectively. Condition (C), requiring a nonempty gap between  $\bar{N}_s^\star$  and  $N_{\rm sl}$ , follows directly from (3a). Assuming  $\Delta_N$  remains nearly constant during the chaotic regime for all  $\kappa$ , and recalling that H' and H'' increase with  $\kappa$ , the last relation in (3b) yields the feedback range  $\mathcal{K}'(\Delta_N) \leq \kappa \leq \mathcal{K}''(\Delta_N)$  that supports LFFs. To find  $\mathcal{K}'$  and  $\mathcal{K}''$ , we substitute H' and H'' in (2a) and (2b) with  $\Delta_N$  and solve them for  $\kappa$ . For example, for  $\Delta_N = 0.047 \cdot 10^{24} \text{/m}^3$  and standard parameters (depicted by bullet I in Fig. 5), we obtain  $\mathcal{K}' \approx 0.082$  and  $\mathcal{K}'' \approx 0.212$ , which define the thick green and red CCM curves in Fig. 4. The corresponding vertical bars in the same figure represent  $H'(\mathcal{K}')$  and  $H''(\mathcal{K}'')$  (both equal to  $\Delta_N$ ) where LFF events can be initiated.

The color maps in Fig. 5 show  $\mathcal{K}'$  and  $\mathcal{K}''$  as functions of  $|r_{\rm f}|^2$  and  $\alpha_{\rm H}$ , estimated using the same  $\Delta_N$ . Within white regions at low  $\alpha_{\rm H}$  Eqs. (3a) or (3b) can not be resolved or conditions (3b) are violated. The upper LFF border  $\mathcal{K}''$  increases with both  $|r_{\rm f}|^2$  and  $\alpha_{\rm H}$ . The lower border  $\mathcal{K}'$  exhibits more complex behavior. While it increases with  $|r_{\rm f}|^2$ , its minimum for given  $\Delta_N$  and fixed  $|r_{\rm f}|^2$  occurs at  $\alpha_{\rm H}\approx 2.5$ . The  $\mathcal{K}'$  and  $\mathcal{K}''$  estimates at bullet I define the thick vertical white bars in Fig. 3, which accurately mark regions with large sub-0.1 GHz peaks in RF spectra and distinct peaks at  $\lambda_{\rm sl}$  in optical spectra. An SLDOF operated at higher injection currents, as modeled here, is preferable for obtaining

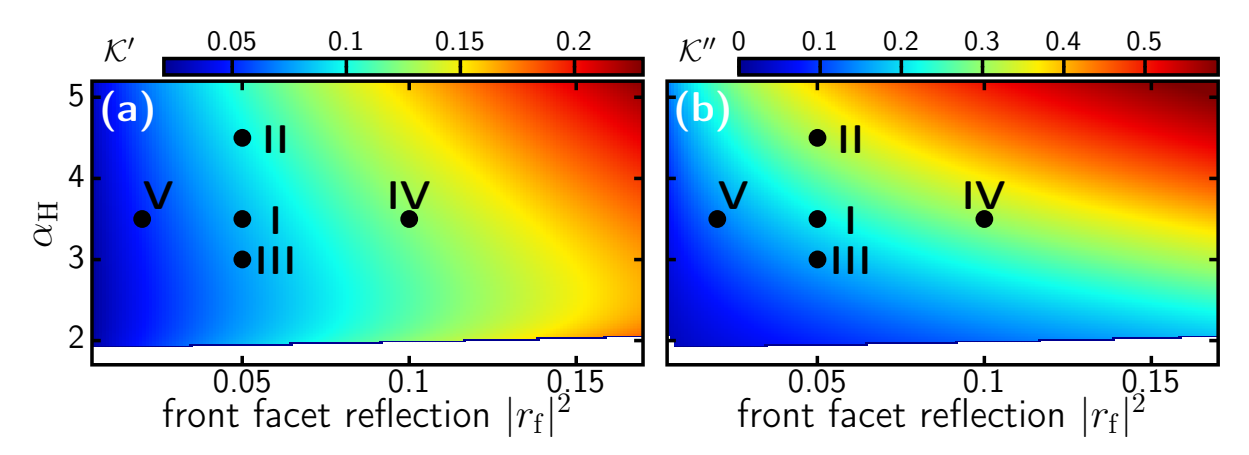


Figure 5: LFF region  $\kappa$ -border estimates  $\mathcal{K}'$  (a) and  $\mathcal{K}''$  (b) as functions of parameters  $|r_{\rm f}|^2$  and  $\alpha_{\rm H}$  for  $\Delta_N=0.047\cdot 10^{24}/{\rm m}^3$ .

more complex chaos at a given optical feedback level in the coherence collapse regime [14, 13]. The onset of LFFs reduces this complexity. Thus, a high value of  $\mathcal{K}'$  is desirable. Fig. 5(a) shows, that a desired setup should have an enhanced front facet reflection, (e.g.,  $|r_{\rm f}|^2>0.15$ ) and  $\alpha_H\approx2.5$ , which should guarantee that  $\mathcal{K}'>0.15$ .

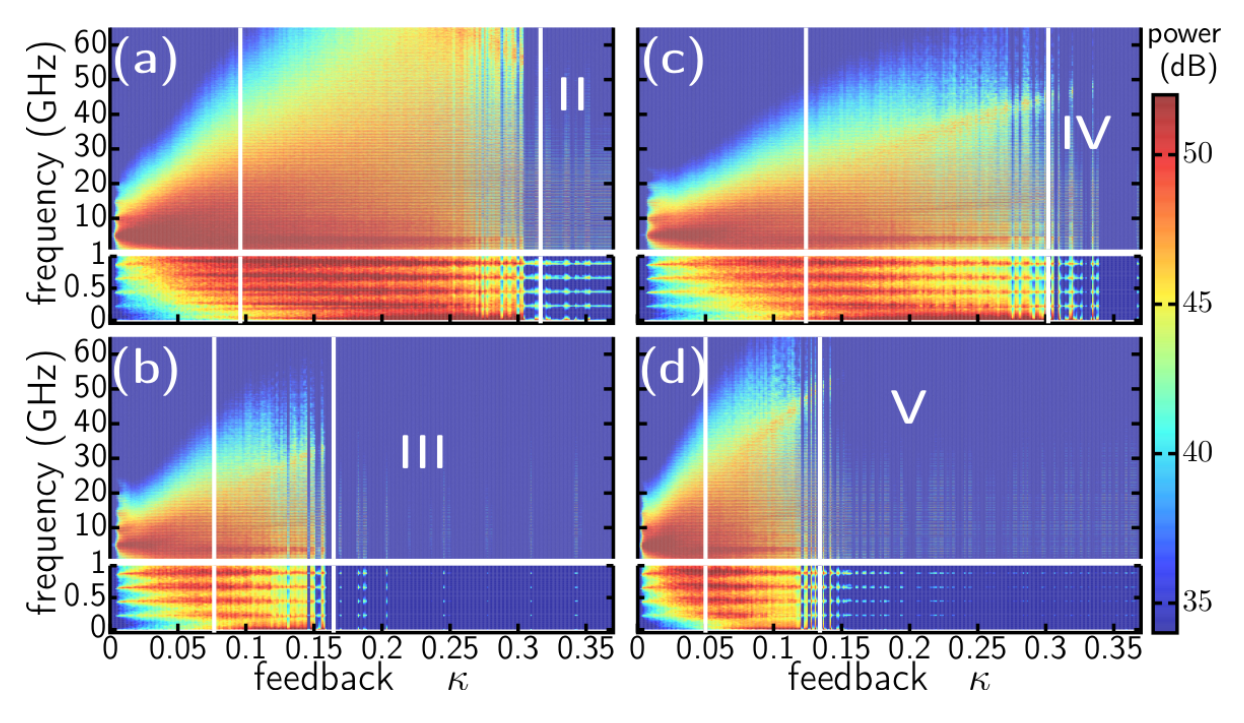


Figure 6: Mappings of the RF-spectra for increased  $\kappa$ , color-coded on a dB scale, for cases II-V from Fig. 5.  $|r_{\rm f}|^2=0.05$  and  $\alpha_{\rm H}=4.5$  (a) or 3 (b);  $\alpha_{\rm H}=3.5$  and  $|r_{\rm f}|^2=0.1$  (c) or 0.02 (d).

To confirm our estimates, we simulated system performance with increasing  $\kappa$  using  $|r_{\rm f}|^2$  and  $\alpha_{\rm H}$  from cases II-V in Fig. 5. The resulting RF-spectral maps are shown in Fig. 6, with the vertical white lines representing LFF border estimates from Fig. 5. These estimates properly predict the LFF regions, indicated by high-intensity peaks below  $0.1\,{\rm GHz}$ . Slight deviations between calculated and estimated LFF ranges could be due to usage of the same  $\Delta_N$  (which should grow with  $I/I_{\rm th}$ ) in all our examples.  $I/I_{\rm th}$  is about 2.21 for cases I, II, and III, but 2.34 for case IV and 2.07 for case V, which is consistent with under- and over-estimation of the LFF ranges in Figs. 6(c) and (d), respectively.

In conclusion, we analyzed the LFF regime of the SLDOF using the TW model and mode analysis. This approach provides a fast way to estimate LFF region boundaries, useful for designing SLDOF systems with broadband chaos. LFFs are much more prevalent than is commonly acknowledged.

# **Appendix**

Below we define the traveling-wave model employed in our simulations, list the standard parameters used, and present the formulas and methods for computing instantaneous optical modes, compound cavity modes (CCMs), and CCM curves in the optical frequency—average carrier density domain.

# Traveling wave model

The 1(space) + 1(time)-dimensional traveling wave (TW) model [18, 15] is based on the TW equations for the slowly varying complex counterpropagating optical fields  $E^+(z,t)$  and  $E^-(z,t)$  in a Fabry-Perot (FP) semiconductor laser (SL), defined for  $z \in (0,l)$ :

$$\left(\frac{n_{\rm g}}{c}\partial_t \pm \partial_z\right)E^{\pm}(z,t) = -i\beta(z,t)E^{\pm}(z,t) + F_{\rm sp}^{\pm}.$$
 (4)

Here, c is the speed of light in vacuum and  $F_{\rm sp}^{\pm}$  represent Langevin noise sources. At the rear (z=0) and front (z=l) facets of the diode, the fields satisfy reflection-reinjection boundary conditions,

$$E^{+}(0,t) = -r_{\rm r}^{*}E^{-}(0,t), \qquad \begin{pmatrix} F_{\rm e}(t) \\ E^{-}(l,t) \end{pmatrix} = \begin{pmatrix} t_{\rm f} & -r_{\rm f}^{*} \\ r_{\rm f} & t_{\rm f} \end{pmatrix} \begin{pmatrix} E^{+}(l,t) \\ F_{\rm i}(t) \end{pmatrix}, \quad t_{\rm f} = \sqrt{1 - |r_{\rm f}|^{2}}, \tag{5}$$

where  $F_{\rm e}$  and  $F_{\rm i}$  denote the emitted and reinjected fields just behind the front facet of the SL, respectively. For the considered SLDOF system, we further assume that these fields are related by

$$F_{\rm i}(t) = \kappa e^{i\varphi} F_{\rm e}(t - \tau), \tag{6}$$

where  $\kappa$  and  $\varphi$  represent the amplitude and phase of the fraction of the emitted field that is reinjected, and the delay time  $\tau$  corresponds to the external cavity (EC) roundtrip time. The field propagation in the EC,  $z \in (l, l+L)$ , with  $L = \frac{c\tau}{2n_{\rm g}}$  denoting the EC length, can also be described by (4). To satisfy (6), we identify the forward and backward fields at the SL-facing side of the EC,  $z = l^+$ , with the emitted and injected fields,  $(E^+(l^+,t),E^-(l^+,t))=(F_{\rm e}(t),F_{\rm i}(t))$ . Within the EC, we assume  $\beta=0$ ,  $n_{\rm g}=1$ , and define the external mirror reflectivity  $r_{\rm ec}$ , which relates the couterpropagating field components via  $E^-(l+L,t)=r_{\rm ec}E^+(l+L,t)$ , as  $\kappa e^{i\varphi}$ .

Within the SL,  $z \in (0, l)$ , the complex field propagation factor  $\beta(z, t)$  in (4) is defined by

$$\beta(z,t) = \beta_0(z,t) - i\frac{\mathcal{D}}{2}, \quad \beta_0(z,t) = i\frac{g_T - \alpha_0}{2} - \frac{\alpha_H g'(N(z,t) - N_{tr})}{2}, \quad g_T = \frac{g'(N(z,t) - N_{tr})}{1 + \varepsilon P(z,t)}.$$
(7)

It depends on the carrier density N(z,t) and, via the total gain function  $g_T$ , on local photon density  $P(z,t)=|E^+|^2+|E^-|^2$ . The linear operator  $\mathcal D$  in (7) describes Lorentzian-shaped material gain dispersion [18],

$$\mathcal{D}E^{\pm} = \bar{g}(E^{\pm} - p^{\pm}), \qquad \frac{\lambda_0^2}{2\pi c} \frac{d}{dt} p^{\pm} = \frac{\bar{\gamma}}{2} (E^{\pm} - p^{\pm}) - i\bar{\lambda}p^{\pm}, \tag{8}$$

where  $p^+(z,t)$  and  $p^-(z,t)$  are the complex linear polarization functions, enabling a straightforward inclusion of frequency dependence in the time-domain model [18]. In the EC, we assume  $\bar{g}=0$ . Finally, the evolution of N is governed by the rate equation [18],

$$\frac{d}{dt}N(z,t) = \frac{1}{ql\sigma} \left( I + \frac{U_F'}{R_s} (\bar{N} - N) \right) - \frac{N}{\tau_N} - \frac{c}{n_g} \Re \sum_{\nu = +} E^{\nu *} \cdot \left( g_T(N,P) - \mathcal{D} \right) E^{\nu}. \tag{9}$$

Here,  $\bar{\mu}$  denotes the spatial average of a spatially distributed function  $\mu(z)$  over the SL, and q is the electron charge. In the simplified model, which neglects gain compression and dispersion and relies on the spatially averaged carrier density  $\bar{N}(t)$ , the propagation factor  $\beta$  is uniform along the SL  $(z\in(0,L))$  and the carrier dynamics is governed by a single ODE:

$$\beta(z,t) \equiv \bar{\beta}(t) = i \frac{(1+i\alpha_{\rm H})g'(\bar{N}(t)-N_{\rm tr})-\alpha_0}{2}, \quad \frac{d}{dt}\bar{N}(t) = \frac{I}{ql\sigma} - \frac{\bar{N}(t)}{\tau_N} - \frac{c}{n_{\rm g}}g'(\bar{N}(t)-N_{\rm tr})\bar{P}(t). \tag{10}$$

The meanings of the model parameters not mentioned before are listed in Table 1 and discussed in detail in [18]. With minor exceptions, all parameter values are identical to those used in [12, 15], and most were adapted from [19].

notation meaning value central wavelength  $830\,\mathrm{nm}$  $\lambda_0$ field roundtrip time in the EC  $4.5\,\mathrm{ns}$  $\tau$ llength of the SL diode  $300 \, \mu \mathrm{m}$  $\sqrt{0.95}$ rear facet (z = -l) reflectivity  $r_{\rm r}$ front facet (z=0) reflectivity  $\sqrt{0.05}$  $r_{\mathrm{f}}$ group velocity factor 3.7  $1.036 \cdot 10^{-20} \, \mathrm{m}^2$ g'differential gain  $10^{24}\,\mathrm{m}^{-3}$  $N_{\rm tr}$ transparency carrier density  $60\,{\rm cm}^{-1}$ field losses in the diode  $\alpha_0$  $5 \,\mu\text{m} \times 0.1 \,\mu\text{m}$ crosssection of the active region  $\sigma$  $2\,\mathrm{ns}$ carrier lifetime  $\tau_{
m N}$  $100\,{\rm cm}^{-1}$ height of the Lorentzian-shaped material gain  $\bar{g}$  $\bar{\gamma}$ full width at half maximum of Lorentzian  $30\,\mathrm{nm}$  $\dot{ar{\lambda}}$ detuning of the material gain peak wavelength  $0\,\mathrm{nm}$  $R_{\rm s}$  $1\Omega$ series resistance  $3.5 \cdot 10^{-26} \, \mathrm{Vm}^3$ derivative of the Fermi level separation  $55\,\mathrm{mA}$ injection current linewidth enhancement factor 3.5  $\alpha_{\rm H}$ 

nonlinear gain compression

fraction of the reinjected field amplitude

reinjected field phase shift

Table 1: Model parameters and their values

 $\varepsilon$ 

 $\kappa$ 

 $\varphi$ 

 $10^{-23}\,\mathrm{m}^3$ 

[0, 0.35]

0

# Instantaneous optical modes

The field equations (4)-(8) for  $z \in SL \cup EC$  can be written in operator form,

$$\begin{split} -i\partial_{t}\Psi(z,t) &= \mathcal{H}(\partial_{z},\beta(N,\varepsilon P))\Psi + F_{\rm sp}(z,t), \quad z \in (0,l) \cup (l,l+L), \quad \text{where} \\ \mathcal{H} &= \begin{pmatrix} \frac{c}{n_{\rm g}}(i\partial_{z} - \beta_{0} + \frac{i\bar{g}}{2}) & 0 & -\frac{c}{n_{\rm g}}\frac{i\bar{g}}{2} & 0 \\ 0 & \frac{c}{n_{\rm g}}(-i\partial_{z} - \beta_{0} + \frac{i\bar{g}}{2}) & 0 & -\frac{c}{n_{\rm g}}\frac{i\bar{g}}{2} \\ -i\frac{\bar{\gamma}}{2}\frac{2\pi c}{\lambda_{0}^{2}} & 0 & (i\frac{\bar{\gamma}}{2} - \bar{\lambda})\frac{2\pi c}{\lambda_{0}^{2}} & 0 \\ 0 & -i\frac{\bar{\gamma}}{2}\frac{2\pi c}{\lambda_{0}^{2}} & 0 & (i\frac{\bar{\gamma}}{2} - \bar{\lambda})\frac{2\pi c}{\lambda_{0}^{2}} \end{pmatrix}, \end{split}$$

$$\Psi(z,t) = \left(E^{+}, E^{-}, p^{+}, p^{-}\right)^{T}, \quad F_{\rm sp}(z,t) = \left(\frac{-ic}{n_{\rm g}}F_{\rm sp}^{+}, \frac{-ic}{n_{\rm g}}F_{\rm sp}^{-}, 0, 0\right)^{T}.$$

Once the propagation factor  $\beta$  is fixed, substituting the Ansatz  $\Psi(z,t)=\Theta(z)e^{i\Omega t}$  into (11) and neglecting the  $F_{\rm sp}$  term yields a spectral problem with respect to the complex eigenfrequency  $\Omega$  and the nontrivial eigenvector  $\Theta(z)=(\Theta_E^+,\Theta_E^-,\Theta_p^+,\Theta_p^-)^T$ :

$$\Omega\Phi(z) = \mathcal{H}(\partial_z, \beta)\Theta(z) \Rightarrow \begin{cases}
\partial_z \Theta_E^{\pm}(z) = \mp i \left[\beta_0 + \frac{\Omega n_{\rm g}}{c} - \frac{i\bar{g}\mu(\Omega)}{2}\right]\Theta_E^{\pm} \\
\Theta_p^{\pm}(z) = \left[1 - \mu(\Omega)\right]\Theta_E^{\pm}(z)
\end{cases}$$
where
$$\mu(\Omega) = \frac{i\left[\Omega + (2\pi c/\lambda_0^2)\bar{\lambda}\right]}{(\pi c/\lambda_0^2)\bar{\gamma} + i\left[\Omega + (2\pi c/\lambda_0^2)\bar{\lambda}\right]},$$
(12)

and the first two components of the vector-function  $\Theta(z)$  satisfy the boundary-interface conditions

$$\zeta_1(0) = -r_{\rm r}^* \zeta_2(0), \quad \zeta_2(l+L) = r_{\rm ec} \zeta_1(l+L), \quad \begin{pmatrix} \zeta_1(l^+) \\ \zeta_2(l) \end{pmatrix} = \begin{pmatrix} t_{\rm f} & -r_{\rm f}^* \\ r_{\rm f} & t_{\rm f} \end{pmatrix} \begin{pmatrix} \zeta_1(l) \\ \zeta_2(l^+) \end{pmatrix}. \quad (13)$$

For each  $\Omega$ , the eigenvector components  $\Theta_E^{\pm}$  can be propagated along the SL and EC using analytically derived transfer matrices. By relating the values of  $\Theta_E^{\pm}$  at the boundaries of these regions and applying the reflection-transmission conditions, we construct a complex characteristic equation [18, 20, 21] with respect to the complex eigenfrequencies  $\Omega$ :

$$\frac{\mathcal{G}(\bar{\beta}_0,\Omega)+1}{\mathcal{G}(\bar{\beta}_0,\Omega)+|r_{\rm f}|^2} = -\frac{\kappa e^{i\varphi-i\Omega\tau}}{r_{\rm f}}, \quad \text{where} \quad \mathcal{G}(\bar{\beta}_0,\Omega) = r_{\rm f}r_{\rm r}^*e^{-i[2\bar{\beta}_0l-i\bar{g}\mu(\Omega)l+\Omega\tau_0]}, \quad \tau_0 = \frac{2ln_{\rm g}}{c}. \tag{14}$$

Once  $\Omega$  is found, the eigenvector components  $\Theta_E^{\pm}(z)$  are reconstructed using the transfer matrices,

$$\begin{pmatrix}
\Theta_E^+ \\
\Theta_E^-
\end{pmatrix}(z'') = \begin{pmatrix}
e^{-i\tilde{\beta}(\Omega,z',z'')} & 0 \\
0 & e^{i\tilde{\beta}(\Omega,z',z'')}
\end{pmatrix} \begin{pmatrix}
\Theta_E^+ \\
\Theta_E^-
\end{pmatrix}(z'),$$

$$\tilde{\beta}(\Omega,z',z'') = \int_{z'}^{z''} \beta_0(z)dz + \left(\frac{\Omega n_{\rm g}}{c} - \frac{i\bar{g}\mu(\Omega)}{2}\right)(z''-z'), \quad z',z'' \in \text{SL or EC},$$
(15)

while  $\Theta_p^{\pm}(z)$  follows from (12). After defining a scalar product

$$(\xi,\zeta) = \sum_{j=1}^{4} n_{g} \int_{0}^{l} \xi_{j}^{*}(z) \zeta_{j}(z) dz + \int_{l}^{l+L} \xi_{j}^{*}(z) \zeta_{j}(z) dz, \tag{16}$$

for four-component vector-functions  $\xi(z)$  and  $\zeta(z)$ , satisfying the boundary-interface conditions

$$\xi_2(0) = -r_{\rm r}\xi_1(0), \quad \xi_1(l+L) = r_{\rm ec}^*\xi_2(l+L), \quad \begin{pmatrix} \xi_2(l^+) \\ \xi_1(l) \end{pmatrix} = \begin{pmatrix} t_{\rm f} & -r_{\rm f} \\ r_{\rm f}^* & t_{\rm f} \end{pmatrix} \begin{pmatrix} \xi_2(l) \\ \xi_1(l^+) \end{pmatrix} \tag{17}$$

and (13), respectively, we construct the adjoint operator  $\mathcal{H}^{\dagger}$  such that  $(\xi, \mathcal{H}\zeta) = (\mathcal{H}^{\dagger}\xi, \zeta)$ :

$$\mathcal{H}^{\dagger} = \begin{pmatrix} \frac{c}{n_{\rm g}} (i\partial_z - \beta_0^* - \frac{i\bar{g}}{2}) & 0 & i\frac{\bar{\gamma}}{2}\frac{2\pi c}{\lambda_0^2} & 0\\ 0 & \frac{c}{n_{\rm g}} (-i\partial_z - \beta_0^* - \frac{i\bar{g}}{2}) & 0 & i\frac{\bar{\gamma}}{2}\frac{2\pi c}{\lambda_0^2}\\ \frac{c}{n_{\rm g}}\frac{i\bar{g}}{2} & 0 & -(i\frac{\bar{\gamma}}{2} + \bar{\lambda})\frac{2\pi c}{\lambda_0^2} & 0\\ 0 & \frac{c}{n_{\rm g}}\frac{i\bar{g}}{2} & 0 & -(i\frac{\bar{\gamma}}{2} + \bar{\lambda})\frac{2\pi c}{\lambda_0^2} \end{pmatrix}.$$
(18)

Each mode  $(\Omega, \Theta(z))$  has a corresponding adjoint counterpart, satisfying

$$\mathcal{H}^{\dagger}\Theta^{\dagger} = \Omega^*\Theta^{\dagger}, \quad \text{where} \quad \Theta^{\dagger}(z) = \left(\Theta_E^{-*}, \Theta_E^{+*}, \frac{\bar{g}\lambda_0^2}{2n_g\bar{\gamma}\pi}\Theta_p^{-*}, \frac{\bar{g}\lambda_0^2}{2n_g\bar{\gamma}\pi}\Theta_p^{+*}\right)^T \tag{19}$$

fulfills (17). For two modes with  $\Omega_l \neq \Omega_k$ , the eigenvectors  $\Theta_l$  and  $\Theta_k^{\dagger}$  are orthogonal,  $(\Theta_k^{\dagger}, \Theta_l) = 0$ . Except at mode degeneracies [22], also known as exceptional points (EPs) [23], where the algebraic multiplicity of a mode exceeds its geometric multiplicity and both (14) and

$$\mathcal{E}(\bar{\beta}_0, \Omega) = (\mathcal{G}(\bar{\beta}_0, \Omega) + 1)^2 - \frac{\tau_0}{\tau} \left[ 1 + \frac{(c\bar{g}/2n_{\rm g})(\pi c/\lambda_0^2)\bar{\gamma}}{[(\pi c/\lambda_0^2)\bar{\gamma} + i[\Omega + (2\pi c/\lambda_0^2)\bar{\lambda}]]^2} \right] \frac{t_{\rm f}^2 \kappa e^{i\varphi - i\Omega\tau}}{r_{\rm f}} \mathcal{G}(\bar{\beta}_0, \Omega) = 0$$
 (20)

are satisfied, the self-product  $(\Theta^\dagger,\Theta)$  remains nonzero. Since  $\frac{\tau_0}{\tau}\ll 1$  in our case, EPs can occur only when  $\mathcal{G}(\bar{\beta}_0,\Omega)\approx -1$ . The sets  $\{\Theta_k(z)\}$  and  $\{\Theta_k^\dagger(z)\}$ , evaluated for the time-dependent distribution  $\beta(z,t)$  obtained during TW model simulations, can then be used to expand the calculated optical field into modal components [20]:

$$\Psi(z,t) = \sum_{k} f_k(t) \Theta_k(z; \beta(z,t)), \qquad f_k(t) = \frac{(\Theta_k^{\dagger}(z), \Psi(z,t))}{(\Theta_k^{\dagger}(z), \Theta_k(z))}. \tag{21}$$

The complex mode amplitudes  $f_k(t)$  and instantaneous mode frequencies  $\Omega_k(\beta(z,t))$  can be used for time-frequency domain representations of the dynamical states [20] in general, and for explaining low-frequency fluctuations [15] in particular. Near an EP, two nearly-degenerated eigenvectors in the mode expansion can be replaced by their properly scaled sum and difference (or by generalized eigenvectors when operating exactly at the EP) [24]. Applying the mode expansion technique to the field equations (11) yields a system of ODEs [20],

$$\frac{d}{dt}f_k = i\Omega_k f_k + \sum_l K_{k,l}(\beta, \Omega_k, \Omega_l) f_l + \zeta_{\rm sp}^{(k)}, \quad K_{k,l} = -\frac{(\Theta_k^{\dagger}, \frac{d}{dt}\Theta_l)}{(\Theta_k^{\dagger}, \Theta_k)}, \quad \zeta_{\rm sp}^{(k)} = i\frac{(\Theta_k^{\dagger}, F_{\rm sp})}{(\Theta_k^{\dagger}, \Theta_k)}, \quad (22)$$

governing the evolution of the mode amplitudes  $f_k$ . In the simplified model, the mode coupling terms are given by  $K_{k,l} = \tilde{K}_{k,l}(\bar{N},\Omega_k,\Omega_l)\frac{d}{dt}\bar{N}$ , where  $\tilde{K}_{k,l} = -(\Theta_k^\dagger,\frac{d\Theta_l}{d\bar{N}})/(\Theta_k^\dagger,\Theta_k)$ , and are available analytically [21]. If the eigenvectors are normalized such that  $\Theta_E^+(l^+)=1$  (so that  $f_k$  in (21) represent mode contributions to the emitted field), these expressions can be written as

$$\bar{K}_{k,l}(\bar{N},\Omega_k,\Omega_l) = \begin{cases} \frac{t_{\mathbf{f}}^2 g' l(1+i\alpha_H) \mathcal{G}(\bar{N},\Omega_k) (\mathcal{G}(\bar{N},\Omega_k)+1)^3 ((\tau+\tau_0) \mathcal{G}(\bar{N},\Omega_k)+(\tau-\tau_0)|r_{\mathbf{f}}|^2)}{2\tau (\mathcal{G}(\bar{N},\Omega_k)+|r_{\mathbf{f}}|^2)^2 \mathcal{E}^2(\bar{N},\Omega_k)} & k=l\\ -\frac{t_{\mathbf{f}}^2 g' l(1+i\alpha_H) (\mathcal{G}(\bar{N},\Omega_k)+1) \sqrt{\mathcal{G}(\bar{N},\Omega_k) \mathcal{G}(\bar{N},\Omega_l)} \sin(\frac{(\Omega_k-\Omega_l)\tau_0}{2}}{i(\mathcal{G}(\bar{N},\Omega_l)+|r_{\mathbf{f}}|^2) \mathcal{E}(\bar{N},\Omega_k) (\Omega_k-\Omega_l)\tau} & k\neq l \end{cases}$$
(23)

Another normalization, which assumes  $(\Theta_k^\dagger,\Theta_k)=1$ , allows to nullify the  $\bar{K}_{k,k}$  terms in (22). Independently of normalization, the complex coupling factors  $\bar{K}_{k,l}$ , which are inversely proportional to the mode frequency separation (typically approximated by  $(2\pi/\tau)$  and its multiples) and the EP-defining function  $\mathcal{E}$ , are generally moderate or small. Consequently,  $\Re\Omega$  and  $\Im\Omega$  usually provide a good representation of a mode's instantaneous relative optical frequency and its damping or amplification rate, even in the presence of other undamped modes. The coupling factors  $\bar{K}_{k,l}$  become significant only when  $|\Omega_k-\Omega_l|\ll 1$  and  $|\mathcal{E}|\ll 1$ , i.e., in the vicinity of an EP.

### Compound cavity modes

When  $\Omega = \omega \in \mathbb{R}$ , i.e.,  $\Im \Omega = 0$ , the instantaneous mode defines the steady state, or compound cavity mode (CCM). For the general TW model, finding CCMs is nontrivial, as it requires constructing

the spatially distributed functions  $\beta(z)$ , P(z), and N(z) that satisfy the stationary (9) [17]. In the simplified TW model, the situation is much simpler:  $\beta(z)$  in (10) is a linear function of the real scalar  $\bar{N}$ , such that the complex characteristic function in (14) depends only on  $\bar{N}$ , the complex  $\Omega$ , and the model parameters. Thus, (14) alone determines the CCM-defining pairs  $(\bar{N},\omega)$ . For  $\kappa=0$  (the solitary SL without feedback), (14) implies

$$\mathcal{G}(N_{\rm sl}, \omega_{\rm sl}) = -1 \implies N_{\rm sl} = N_{\rm tr} + \frac{\alpha_0 l - \ln|r_{\rm f} r_{\rm r}|}{g' l}, \omega_{\rm sl} = \frac{\arg(-r_{\rm f} r_{\rm r}^*) + \alpha_{\rm H}(\alpha_0 l - \ln|r_{\rm f} r_{\rm r}|)}{\tau_0} \mod \frac{2\pi}{\tau_0}, \tag{24}$$

where the unique  $N_{\rm sl}$  is the threshold carrier density, while the multiple  $\omega_{\rm sl}$  are Fabry-Perot resonance frequencies separated by  $(2\pi/\tau_0)$ .

A fast method to find CCMs in the  $\Re\Omega/\bar{N}$  domain has been discussed, e.g., in [20, 18, 17]. It is based on separately considering the real amplitudes and phases of the terms on both sides of (14). After introduction of the carrier density and frequency offsets,  $\Delta\bar{N}=\bar{N}-N_{\rm sl}$  and  $\Delta\omega=\omega-\omega_{\rm sl}$ , the resulting conditions can be written as

$$|r_{\rm f}| \frac{|e^{g'l\Delta\bar{N}}e^{i(\alpha_{\rm H}g'l\Delta\bar{N}-\Delta\omega\tau_0)}-1|}{|e^{g'l\Delta\bar{N}}e^{i(\alpha_{\rm H}g'l\Delta\bar{N}-\Delta\omega\tau_0)}-|r_{\rm f}|^2|} = \kappa,$$

$$(\omega_{\rm sl}\tau + \pi + \arg r_{\rm f}) + \Delta\omega\tau + \arg \frac{e^{(1+i\alpha_{\rm H})g'l\Delta\bar{N}-i\Delta\omega\tau_0}-1}{e^{(1+i\alpha_{\rm H})g'l\Delta\bar{N}-i\Delta\omega\tau_0}-|r_{\rm f}|^2} = \varphi \mod 2\pi.$$
(25)

Here,  $\kappa$  and  $\varphi$  are expressed explicitly as functions of  $\Delta\omega$  and  $\Delta\bar{N}$ . For fixed  $\kappa$ , the first relation in (25) defines pairs  $(\Delta\omega,\Delta\bar{N})$  of CCMs lying along  $\varphi$ -parametrized curves. Alternatively, for fixed  $\varphi$ , the second relation defines  $\kappa$ -parametrized CCM curves. Within a bounded  $\Delta\omega/\Delta\bar{N}$  domain, these curves can be traced using continuation techniques [17], and their intersections specify the CCM positions. For the present SLDOF system, the first condition in (25) allows deriving explicit formulas for  $\varphi$ -parametrized, fixed- $\kappa$  CCM curves [15]:

$$\Delta\omega = \frac{\alpha_{\rm H}g'l}{\tau_0} \Delta \bar{N} \pm \frac{1}{2} W(\Delta \bar{N}) \mod \frac{2\pi}{\tau_0}, \text{ where}$$

$$W(\Delta \bar{N}) = \frac{2}{\tau_0} \arccos \frac{\cosh(g'l\Delta \bar{N}) - \kappa^2 \cosh(g'l\Delta \bar{N} - \ln|r_{\rm f}|^2)}{1 - \kappa^2}.$$
(26)

Here,  $W(\Delta \bar{N})$  denotes the width of the CCM-curve in the  $\Re\Omega/\bar{N}$  domain at the given "height"  $\Delta \bar{N}$ . The minima of these curves, where W vanishes, define the position of the maximal-gain mode (MGM)  $(\Delta\omega_{\rm mg},\Delta N_{\rm mg})$  on the CCM-curve [15]:

$$\Delta\omega_{\rm mg} = -\frac{\alpha_{\rm H}}{\tau_0} \ln\left(\frac{1+\kappa/|r_{\rm f}|}{1+\kappa|r_{\rm f}|}\right), \qquad \Delta N_{\rm mg} = \frac{\tau_0 \Delta\omega_{\rm mg}}{\alpha_{\rm H}g'l}. \tag{27}$$

We note that (26) and (27) completely ignore the length of the EC (the formulas are independent on  $\tau$ ). Consequently, for short compound cavities (see, e.g., [20, 18]), the MGM defined at a fixed feedback phase  $\varphi$  can be significantly shifted relative to the one predicted by (27). In such short cavities, the feedback phase  $\varphi$  plays a crucial role in determining the system dynamics. This is not a concern for the long external cavity system modeled in the associated manuscript.

# References

- [1] D.M. Kane and K.A. Shore, editors. *Unlocking Dynamical Diversity: Feedback Effects on Semi-conductor Lasers*. John Wiley & Sons, 2005.
- [2] J. Ohtsubo. *Semiconductor Lasers: Stability, Instability and Chaos.* Springer Series in Optical Sciences. Springer, 4 edition, 2017.

- [3] Miguel C. Soriano, Jordi García-Ojalvo, Claudio R. Mirasso, and Ingo Fischer. Complex photonics: Dynamics and applications of delay-coupled semiconductors lasers. *Reviews of Modern Physics*, 85:422–470, 2013.
- [4] J. Mork, B. Tromborg, and J. Mark. Chaos in semiconductor lasers with optical feedback: theory and experiment. *IEEE J. Quant. Electron.*, 28(1):93–108, 1992.
- [5] T. Sano. Antimode dynamics and chaotic itinerancy in the coherence collapse of semiconductor lasers with optical feedback. *Phys. Rev. A*, 50:2719–2726, 1994.
- [6] G.H.M. van Tartwijk, A.M. Levine, and D. Lenstra. Sisyphus effect in semiconductor lasers with optical feedback. *IEEE J. Sel. Topics Quantum Electron.*, 1:466–472, 1995.
- [7] B. Tromborg, J. Mork, and V Velichansky. On mode coupling and low-frequency fluctuations in external-cavity laser diodes. *Quantum and Semiclassical Optics*, 9(5):831–851, 1997.
- [8] Andreas Karsaklian Dal Bosco, Shoma Ohara, Naoki Sato, Yasuhiro Akizawa, Atsushi Uchida, Takahisa Harayama, and Masanobu Inubushi. Dynamics versus feedback delay time in photonic integrated circuits: Mapping the short cavity regime. *IEEE Photonics Journal*, 9(2):1–12, 2017.
- [9] Ming-Wei Pan, Bei-Pei Shi, and G.R. Gray. Semiconductor laser dynamics subject to strong optical feedback. *Opt. Lett.*, 22(3):166–168, 1997.
- [10] Fadwa Baladi, Min Won Lee, Jean-René Burie, Mauro A. Bettiati, Azzedine Boudrioua, and Alexis P. A. Fischer. High-resolution low-frequency fluctuation map of a multimode laser diode subject to filtered optical feedback via a fiber bragg grating. *Opt. Lett.*, 41(13):2950–2953, Jul 2016.
- [11] Kazuto Yamasaki, Kazutaka Kanno, Atsushi Matsumoto, Kouichi Akahane, Naokatsu Yamamoto, Makoto Naruse, and Atsushi Uchida. Fast dynamics of low-frequency fluctuations in a quantumdot laser with optical feedback. *Opt. Express*, 29(12):17962–17975, Jun 2021.
- [12] M. Radziunas, D.J. Little, and D.M. Kane. Numerical study of optical feedback coherence in semiconductor laser dynamics. *Optics Letters*, 44(17):4207–4210, 2019.
- [13] Deb M Kane and Mindaugas Radziunas. Chaotic semiconductor laser systems—bandwidth enhancement predicted by numerical simulations. *Laser Physics Letters*, 22(9):096201, sep 2025.
- [14] J.P. Toomey and D.M. Kane. Mapping the dynamic complexity of a semiconductor laser with optical feedback using permutation entropy. *Optics Express*, 22(2):1713–1725, 2014.
- [15] M. Radziunas and D. Kane. Traveling wave mode analysis of a coherence collapse regime semi-conductor laser with optical feedback. *J. of the Opt. Soc. of America B*, 41(11):2638–2647, 2024.
- [16] R. Lang and K. Kobayashi. External optical feedback effects on semiconductor injection laser properties. *IEEE J. Quantum Electron.*, 16(3):347–355, 1980.
- [17] M. Radziunas. Calculation of the steady states in dynamic semiconductor laser models. *Optical and Quantum Electronics*, 55:121, 2023.
- [18] M. Radziunas. Traveling wave modeling of nonlinear dynamics in multisection semiconductor laser diodes. In J. Piprek, editor, *Handbook of Optoelectronic Device Modeling and Simulation: Lasers, Modulators, Photodetectors, Solar Cells, and Numerical Methods*, volume 2, chapter 31, pages 153–182. CRC Press, 2017.

- [19] R. Ju, Y. Hong, and P. Spencer. Semiconductor lasers subject to polarisation-rotated optical feedback. *IEE Proceedings Optoelectronics*, 153(3):131–137, 2006.
- [20] M. Radziunas and H.-J. Wünsche. Multisection lasers: Longitudinal modes and their dynamics. In J. Piprek, editor, *Optoelectronic Devices Advanced Simulation and Analysis*, chapter 5, pages 121–150. Springer, 2005.
- [21] M. Radziunas. Numerical bifurcation analysis of the traveling wave model of multisection semi-conductor lasers. *Physica D: Nonlinear Phenomena*, 213(1):98–112, 2006.
- [22] H. Wenzel, U. Bandelow, H.-J. Wünsche, and J. Rehberg. Mechanisms of fast self pulsations in two-section DFB lasers. *IEEE J. of Quantum Electron.*, 32(1):69–78, 1996.
- [23] M. Liertzer, Li Ge, A. Cerjan, A.D. Stone, H. E. Türeci, and S. Rotter. Pump-induced exceptional points in lasers. *Phys. Rev. Lett.*, 108:173901, 2012.
- [24] J. Sieber. Numerical bifurcation analysis for multisection semiconductor lasers. *SIAM J. on Appl. Dyn. Systems*, 1(2):248–270, 2002.